Manufacture and buckling test of a variable-stiffness, variable-thickness composite cylinder under axial compression

Reece L. Lincoln*, Paul M. Weaver†, Alberto Pirrera‡, and Rainer M. J. Groh§
Bristol Composites Institute, University of Bristol, UK

Variable-angle tow (VAT) manufacturing methods significantly increase the design space for elastic tailoring of composite structures by smoothly changing the fiber angle and thickness across a component. Rapid Tow Shearing (RTS) is a VAT manufacturing technique that uses in-plane shearing (rather than in-plane bending) to steer tows of dry or pre-impregnated fibers. RTS offers a number of benefits over conventional bending-driven steering processes, including tessellation of adjacent tow courses; no overlaps or gaps between tows; and no fiber wrinkling or bridging. Further to this, RTS offers an additional design variable: fiber orientation-to-thickness coupling due to the volumetric relation between tow shearing and the tow thickness and width. Previous computational work has shown that through a judicious choice of curvilinear fiber trajectories along a cylinder's length and across its circumference, the imperfection sensitivity of cylindrical shells under axial compression can be reduced and load-carrying capacity increased. The present work aims to realize these predictions by manufacturing and testing two cylinders: an RTS cylinder and a straight-fiber quasi-isotropic cylinder as a benchmark. The tow-steered manufacturing process, imperfection measurements, instrumentation, and buckling tests of both cylinders are discussed herein. The experimental tests results are compared against high-fidelity geometrically nonlinear finite element models that include measured imperfections before and during the tests. Finally, we discuss outstanding challenges in designing and manufacturing RTS cylinders for primary aerostructures.

Nomenclature

L	=	length
m	=	mass
r	=	inner radius of cylinder
t^k, t_0^k	=	local ply thickness and nominal ply thickness of the k^{th} layer, respectively
T_0^k, T_1^k	=	initial and final shearing angle of a period of the k^{th} layer, respectively
n^k	=	periodicity of the k^{th} layer
θ^k	=	local shearing angle in the k^{th} layer
ρ	=	density
ϕ^k	=	direction of shearing of the k^{th} layer

I. Introduction

To enable the next generation of lightweight launch-vehicle structures, composite materials are a promising avenue towards further optimization, owing to their high levels of customization through specific fiber angle placement [1, 2]. Further to this already enlarged design space compared to metals, variable-angle tow (VAT) manufacturing techniques offer even more flexibility in structural design as the trajectory of individual tows (fiber courses of finite width) can be varied smoothly and continuously across a part. In general, the ability to place curvilinear fiber paths enables load paths to be tailored across a structure.

*PhD Researcher, Bristol Composites Institute, University of Bristol, UK
†Professor in Lightweight Structures, Bristol Composites Institute, University of Bristol, UK and Bernal Chair of Composite Materials and Structures, School of Engineering, University of Limerick, Castletroy, Ireland
‡Associate Professor in Nonlinear Structural Mechanics, Bristol Composites Institute, University of Bristol, UK
§Lecturer in Digital Engineering of Structures, Bristol Composites Institute, University of Bristol, UK

One such VAT manufacturing technique is Continuous Tow Shearing (CTS) [3, 4], which was specifically developed to overcome manufacturing defects induced by Automated Fiber Placement (AFP) processes during steering. CTS was developed further by iCOMAT Ltd. [5] into Rapid Tow Shearing (RTS), a derivative of CTS with a higher deposition rate*. Unlike AFP, which relies on in-plane bending of tows, RTS uses in-plane shearing to change the tow direction continuously as the tow is placed. This shearing-dominated steering process allows perfect tessellation of tow courses, eliminates fiber wrinkling or straightening, and removes the need for tow gaps or overlaps. In addition, RTS introduces a new design variable: fiber orientation-to-tow thickness coupling. In order to conserve volume, the shearing action causes a local build-up in thickness and reduction in tape width as the tow is steered. The relationship between shearing angle θ^k and local thickness t^k is given by

$$t^k = \frac{t_0^k}{\cos\theta^k} \tag{1}$$

where t_0^k is the nominal ply thickness of the k^{th} ply. The maximum shearing angle, given by manufacturing constraints, is $\theta_{\max}^k = 70°$ [6]. A shearing angle of 70° results in a local thickness of three times the nominal ply thickness. The fiber angle-to-tow thickness coupling therefore allows unique opportunities for design. For example, by periodically and repeatedly shearing a tow between two orientations along a cylinder's length or across the cylinder's circumference, embedded stiffeners can be manufactured *in-situ* [7].

In the case of an axially compressed cylindrical shell, it is desirable to create a composite cylinder with embedded stringers, rings, ortho-grids or even iso-grids. Previous work has found that in finite element (FE) predictions RTS cylinders have an increased specific buckling load when compared to their straight-fiber counterparts [8]. When modeled stochastically with Monte Carlo simulations of nonlinear buckling analyses and a dataset of measured geometric imperfections, RTS cylinders also showed a smaller variance and higher mean buckling load when compared to straight-fiber cylinders [7]. As a result, the well-documented sensitivity to geometric imperfections of axially compressed cylindrical shells was shown to be smaller for RTS cylinders. Tow-steering therefore creates the possibility of designing inherently imperfection-insensitive cylinders, and possible mass and monetary savings in launch-vehicle structural design.

A. Related Work

In general, tow-steering has been shown to improve the mechanical properties of shells. Hyer and Charette [9] were among the first to investigate the benefits of a variable-stiffness architectures and found that a variable-stiffness laminate increased the tensile strength of a laminate with a hole by 100% when compared to a unidirectional design. The benefits of variable-stiffness extend beyond tensile strength, as demonstrated by White and Weaver [10], who showed that by using variable-stiffness composites the buckling behavior of a cylindrical panel could be converted from imperfection sensitive and shell-like to imperfection insensitive and plate like. Wu et al. [11] manufactured and tested tow-steered composite shells using AFP. Results indicate that the non-uniform pre-buckling membrane stress field due to tow-steering causes a reduced sensitivity to imperfections. The post-buckling response of this tow-steered cylinder was further studied by White *et al.* [12]. One of the tow-steered cylinders investigated showed a consistent, small (relative to the circumference of the cylinder) dimple that had a limited impact on the post-buckling regime from the "direct membrane load path through the structure" [12] when compared to a tow-steered cylinder that had a relatively large dimple. Further research on these shells indicated that even with small [13] and large [14] cutouts, the shells maintain 91–92% of the axial stiffness and 85–86% of the buckling load when compared to the pristine shell. Blom [15] designed, manufactured, and tested a variable-stiffness composite shell in bending. Blom found a re-distributed strain field resulted in 10 and 35% lower strains for the compressive and tensile strains when compared to a baseline cylinder (straight-fiber laminae at 0, 90 and ±45 degree).

Following previous work on optimizing the imperfect, specific buckling load of axially compressed cylinders using RTS-enabled tow steering [7], the aim of this paper is to validate the model predictions in experimental tests. To do so, one quasi-isotropic straight-fiber cylinder and one optimized RTS steered cylinder were manufactured, which are then characterized and tested in axial compression.

B. Paper Organization

The structure of this paper is as follows. Section II details the notation of an RTS-manufactured lamina and nuances of a RTS-manufactured cylinder, while Section III describes the QI and RTS cylinder manufacturing process, sample

*RTS is the manufacturing technique used within the present work and is referred to herein.

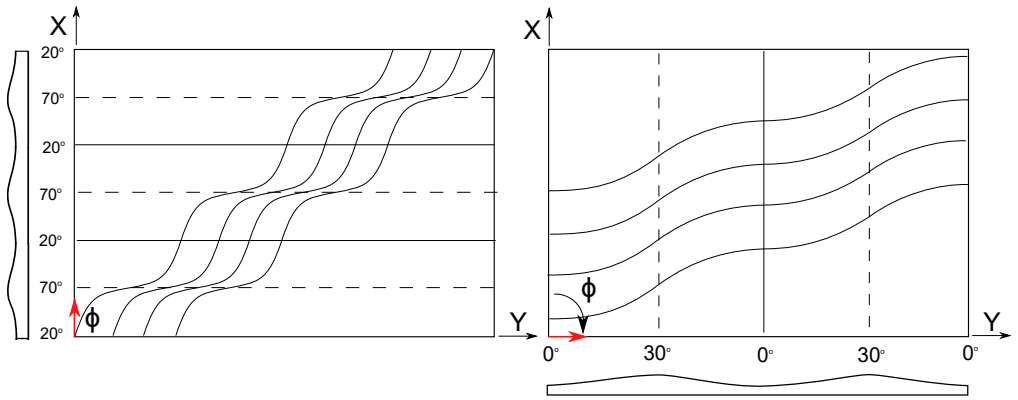

Fig. 1 A single ply of steered composite using RTS on an 'unrolled' cylinder planform. (a) Steering along the cylinder length from $20°$ to $70°$ (with respect to the X-axis) over three periods. (b) Steering across the cylinder circumference from $0°$ to $30°$ (with respect to Y-axis) over two periods. The corresponding increase in thickness for both plies is shown in cross-sectional views. Using the notation of Eq. (2) the fiber orientation is described by (a) $0\langle 20|70\rangle^3$ and (b) $90\langle 0|30\rangle^2$.

preparation steps and pre-test finite element (FE) predictions. Section IV covers the axial compression test setup and results for both QI and RTS cylinders. Section V details the correlation of experimental results against FE predictions. Section VI concludes the paper with a brief summary of results and areas of future work.

II. RTS Notation

To define the k^{th} layer of a RTS ply, an adapted version of the nomenclature from Gürdal and Olmedo's [16] seminal paper on VAT composites is used

$$\phi^k \langle T_0^k | T_1^k \rangle^{n^k} \tag{2}$$

where ϕ^k is an angle measured counterclockwise from the global x-axis and is the axis that defines the direction of steering. To create a ply without gaps or overlaps individual steered tows need to be shifted perpendicular to ϕ^k. T_0^k is the initial shearing angle, measured counterclockwise from the ϕ^k axis. T_1^k is the final angle of shearing, measured counterclockwise from the ϕ^k axis. n^k is an adaptation of the aforementioned nomenclature by Gürdal and Olmedo and defines the periodicity, i.e., how many $T_0^k \rightarrow T_1^k \rightarrow T_0^k$ cycles occur in the ϕ^k direction. The maximum possible periodicity of a ply is defined by the minimum steering radius of RTS (assumed to be 50 mm based on RTS process characterization) and the length of the cylinder in the ϕ^k direction.

Interestingly, the mass of an RTS cylinder that has periodic shearing as defined above is independent of the periodicity (n^k), and only a function of the T_0 and T_1 shearing angles. As the periodicity is directly related to the number of thickness build-ups (see Fig. 1), the independence of mass in relation to number of thickness build-ups is in direct contrast to the typical use of stiffeners where more stiffeners typically increases mass. The mass m of a RTS cylinder can be calculated by

$$m = 2\pi r L \rho \sum_{k=1}^{N} \left(\left(\frac{t_0^k}{T_1^k - T_0^k} \right) \int_{T_0^k}^{T_1^k} \sec(u) \mathrm{du} \right) \tag{3}$$

where r is the radius of the cylinder, L is the length of the cylinder, ρ is the density of the composite material, and shearing angles T_0^k and T_1^k are in radians.

III. Manufacture and Predictions

Two cylinders were manufactured as part of this study. The first is an eight-ply quasi-isotropic (QI) straight-fiber layup with stacking sequence $[\pm 45, 0, 90]_s$, which serves as a benchmark ($0°$ plies have the fibers aligned with the cylinder axis, and $90°$ plies with the cylinder circumference). The second cylinder is a steered RTS cylinder with

Table 1 Nominal material properties of the composite cylinders manufactured. Material properties are from [17].

E_{11} [GPa]	E_{22} [GPa]	ν_{12} -	G_{12} [GPa]	ρ [g/cm^3]
138	9.72	0.356	4.69	1.57

an eight-ply stacking sequence $\left[0 \pm \langle 20|25\rangle^2, 90 \pm \langle 35|25\rangle^9\right]_s$ that was determined in a previous optimization study to maximize the mass-specific buckling load in a nonlinear finite element analysis that accounted for geometric imperfections [7]. Both composite cylinders have a nominal inner radius of 300 mm, a nominal unpotted length of 1100 mm, and a nominal (unsheared) thickness of 1.05 mm. For the RTS cylinder, the thickest part due to the fiber orientation-to-ply thickness coupling is 1.21 mm with an average thickness of 1.17 mm. Both cylinders are manufactured using the aerospace-grade pre-preg IM7/8552. Nominal material properties are listed in Table 1.

A. Sample manufacture

As shown in Fig. 2, the cylinders were manufactured by placing courses of adjacent tows (straight for the QI and steered for the RTS cylinder) to form a ply on a flat tooling plate. Following industry practice, adjacent tows were not allowed to overlap and have a maximum gap of 2 mm. Each flat ply is then individually wrap-rolled onto an aluminum tool mandrel, and then debulked. A thorough quality assurance process was carried out for each ply and any minor defects were either removed (e.g. with the help of a heat gun) or noted. Curing of the wrapped QI and RTS cylinders was then conducted in an autoclave and according to the material supplier's specifications.

B. Sample preparation

Once cured, end-potting with a nominal depth of 30 mm was applied to both ends of the cylinder using Araldite epoxy. The end-potted cylinder is shown in Fig. 3.

The epoxy end-potting was faced by shaving up to 1 mm from both ends of the cylinder to ensure that the two surfaces where boundary conditions are applied in the axial compression tests are parallel. All specified tolerances—±0.25 mm for parallelism and flatness and ±1.000 mm for perpendicularity—were achieved. After facing, metrology measurements were carried out by using a computer-controlled coordinate measurement machine (CMM) probe at 20,000 points across both cylinder surfaces (approximately every 10 mm in both the circumferential and axial directions). Data from the CMM were used to inform on the manufacturing quality and also used as inputs to the nonlinear finite element analyses with the as-manufactured imperfection signature. Following best practice in the experimental literature [18–20], to post-process these data, a cylinder of best fit is first fitted to the 20,000-point data cloud by minimizing the root mean square of the imperfection data cloud against the best fit cylinder. The best fit QI cylinder has an outer radius of 302.20 mm, 1.15 mm larger than the designed outer radius. The best fit RTS cylinder has an outer radius of 302.11 mm, 0.94 mm larger than the designed outer radius. The results of the QI and RTS cylinder CMM are shown in Fig. 4.

The RTS cylinder has a maximum imperfection amplitude of 8.30 mm, 1.79 times greater than the maximum imperfection amplitude of the QI cylinder of 4.63 mm. Deviations in the cylinder wall profile are most likely due to: (i) tool-part interaction during curing in the autoclave, (ii) spatial non-uniformity in cool down of the part at the end of the curing cycle, and (iii) the single weld seam in the aluminum tooling mandrel that, while machined to be within high tolerance, leads to differential thermal expansion in the autoclave. Manufacturing imperfections are also likely compounded by the variable stiffness (and therefore variable coefficients of thermal expansion) of the RTS cylinder. Imperfections introduced by these factors are commonly observed in manufacturing of composite cylinders, which is why, compared to metallic cylinders, composite cylinders often feature lower-order periodic imperfections (i.e., ovalizations) rather than higher-order periodic imperfections (i.e., high-frequency surface waviness) [21–24]. Indeed, the dominant imperfection signature for the both cylinders is an ovalization mode, which is shown in Fig. 4.

A speckle pattern was sprayed onto each cylinder to take surface deflection and strain measurements during the experimental tests using a two-camera digital image correlation (DIC) system. The location of DIC was informed by FE predictions. Four linear variable differential transformers (LVDTs) were placed at 90° increments around the circumference of the cylinder to measure the eccentricity of loading. Strain gauges were also instrumented at nine and twelve locations across the QI and RTS cylinder, respectively, to complement and corroborate DIC measurements. The locations of DIC and strain gauges for the QI and RTS cylinders are shown in Fig. 5.

(a) Manufacturing Process

(b) Cured QI Cylinder

Fig. 2 The manufacturing process uses wrap-rolling by depositing multiple tows in adjacent courses onto a flat tooling surface to create a full ply, and then wrapping each individual ply carefully around the cylinder creating a butt joint at the seam. Butt joints of individual plies are staggered around the circumference in 45° intervals. Two cylinders are manufactured (one CTS steered and one QI straight fiber) and cured in an autoclave.

C. Finite Element Analyses

Prior to the test, FE analyses of the QI and RTS cylinders with as-manufactured imperfections were carried out to predict the buckling load and axial stiffness of the cylinders. The coordinate system to define the cylinder geometry and imperfections is shown in Fig. 6. The imperfection measurements were carried out between $x = 40$ mm and $x = 1060$ mm 93% of the unpotted length of the cylinder (0 to 24 mm and 1074 mm to 1098 mm is the end-potted region). Following best practice in the literature [18–20], the imperfection data cloud was deconstructed into Fourier coefficients and magnitudes based on a full four-term Fourier series decomposition. Once achieved, the Fourier series can be used to extrapolate the imperfections from $x = 50$ mm to $x = 24$ mm (the start of the bottom end-potting) and from $x = 1060$ mm to $x = 1074$ mm (the start of the top end-potting).

For two coordinates (x, y), in this case the axial and circumferential coordinates, that have been scaled to the domain [-π,π], the imperfection variable $f(x, y)$ can be represented by the following Fourier series,

$$f(x,y) = \sum_{m,n}^{\infty} \lambda_{mn} \Big[A_{mn} \cos(mx)\cos(ny) + B_{mn} \sin(mx)\cos(ny) + C_{mn} \cos(mx)\sin(ny) + D_{mn} \sin(mx)\sin(ny) \Big] \quad (4)$$

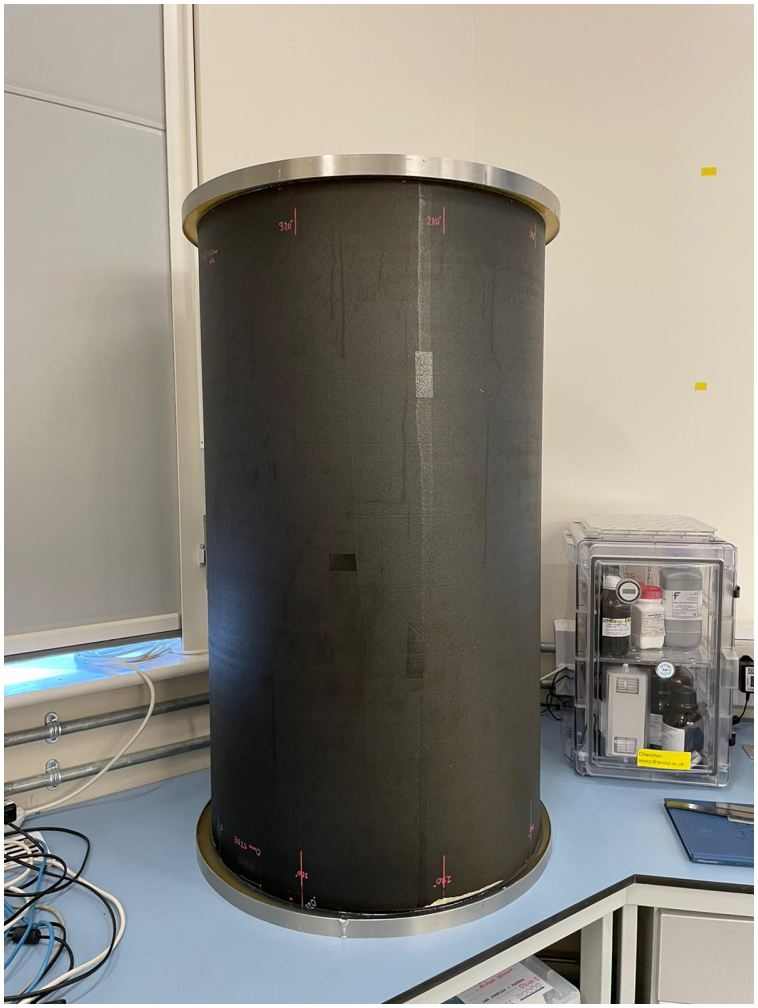

Fig. 3 End-potted QI cylinder.

where

$$A_{mn} = \frac{1}{\pi^2} \iint_{-\pi}^{\pi} f(x,y) \cos(mx) \cos(ny)\, \mathrm{d}x\, \mathrm{d}y \,, \tag{5}$$

$$B_{mn} = \frac{1}{\pi^2} \iint_{-\pi}^{\pi} f(x,y) \sin(mx) \cos(ny)\, \mathrm{d}x\, \mathrm{d}y \,, \tag{6}$$

$$C_{mn} = \frac{1}{\pi^2} \iint_{-\pi}^{\pi} f(x,y) \cos(mx) \sin(ny)\, \mathrm{d}x\, \mathrm{d}y \,, \tag{7}$$

$$D_{mn} = \frac{1}{\pi^2} \iint_{-\pi}^{\pi} f(x,y) \sin(mx) \sin(ny)\, \mathrm{d}x\, \mathrm{d}y \,, \tag{8}$$

and

$$\lambda_{mn} = \begin{cases} 0.25 \text{ for } m = n = 0 \\ 0.5 \text{ for } m > 0, n = 0, \text{ or } m = 0, n > 0 \\ 1 \text{ for } m > 0, n > 0. \end{cases}$$

For both CMM data clouds, a decomposition using $m = 51$ (axial direction) and $n = 21$ (circumferential) modes was used to converge the Fourier series. Final convergence was based around locally converging both the maximum

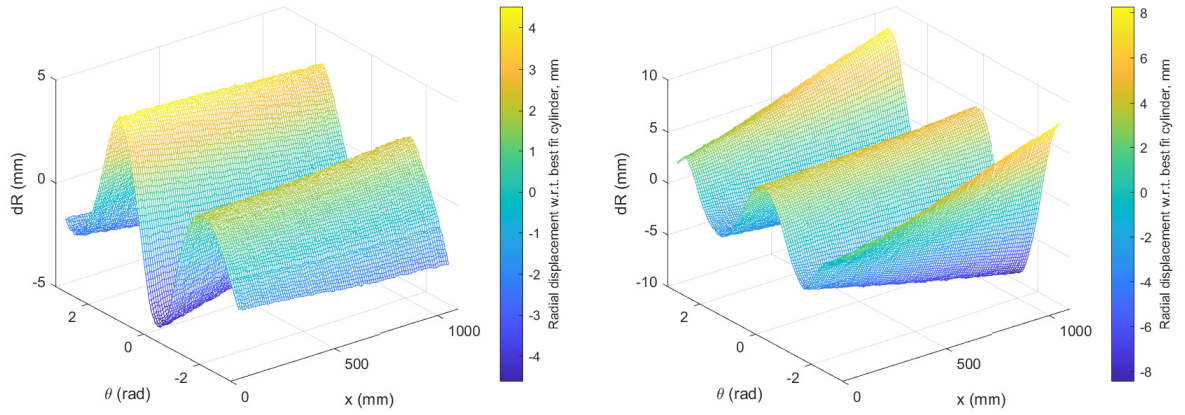

(a) (b)

Fig. 4 QI (a) and RTS (b) as-manufactured radial imperfections from CMM data collection. Radial deflection is plotted with respect to a best fit cylinder of the CMM data cloud.

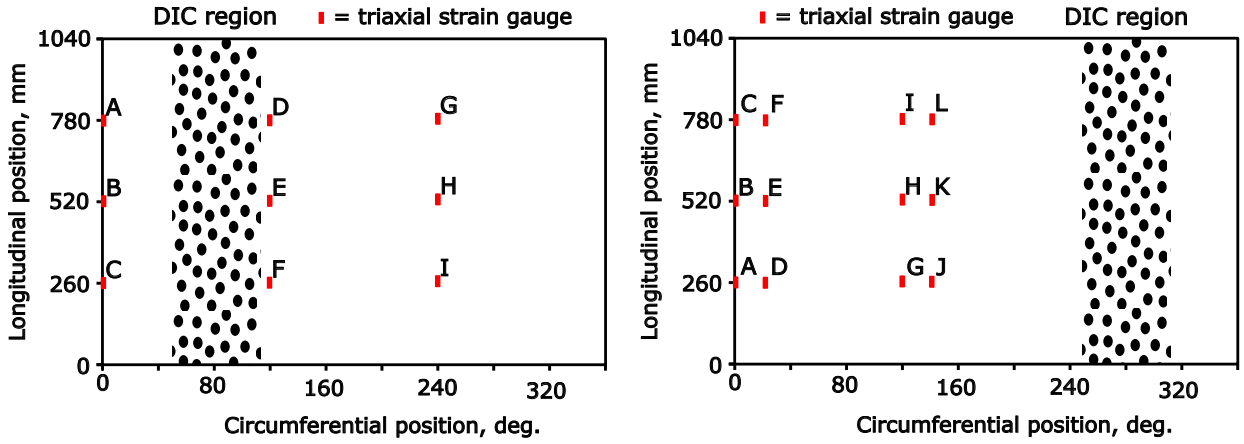

(a) (b)

Fig. 5 QI (a) and RTS (b) strain gauge and DIC location.

and minimum value of the (m, n) imperfection magnitudes, ζ_{mn}, to within 0.1% where the imperfection magnitude is defined by

$$\zeta_{mn} = \sqrt{A_{mn}^2 + B_{mn}^2 + C_{mn}^2 + D_{mn}^2}. \tag{9}$$

The contributions of the different Fourier modes for both QI and RTS cylinders in the axial, m, and circumferential, n, directions are plotted with their magnitude λ_{mn} in Fig. 7.

It is clear that the dominant imperfection mode is an ovalization mode ($\zeta_{0,2}$), as $m = 0$ represents no undulation along the length and $n = 2$ represents a full wave around the circumference. Hence, the Fourier decomposition reflects the visual inspection of Fig. 4 for both cylinders. The relative magnitude of the different Fourier modes in Fig. 7 is common for composite cylinders with decreasing importance as m and n increase, as has been observed in previous studies [25].

The Fourier modes shown in Fig. 7 were applied to modify the coordinates of nodes within the FE mesh. The modified mesh was used in a geometrically nonlinear buckling analyses in Abaqus/CAE, based on Python-scripted input files developed in previous work [7, 8] to define fiber-angle and thickness distributions for the CTS cylinder. The boundary conditions applied in these models replicates the test boundary conditions (clamped) as closely as possible, including the stiffening effect of the end-potting.

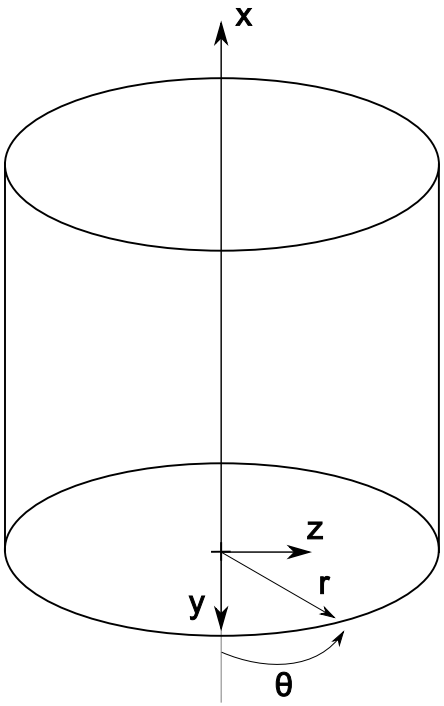

Fig. 6 Coordinate system to define cylinder geometry.

Table 2 Planar model material properties for epoxy and aluminum.

	E	ν	G
	[GPa]	-	[msi]
Epoxy	3	0.3	2.14
Aluminum	70	0.3	70

1. Planar model

To account for the end-potting, a 2D FE planar model was created to find the local stiffening effect of the potting material. The 2D planar model by White et al. [12] and Hilburger and Starnes Jr. [26] was used as it represents the standard means of assessing the influence of end-potting. The local stiffening due to the encasement is unlikely to affect the buckling load, but has been shown to have a small (1–5%) effect on pre-buckling stiffness. An accurate prediction of pre-buckling stiffness is key to correlate nonlinear analyses and experimental results. By considering a cross-sectional cut of the encased area, a half-model can be created. The model is shown in Fig. 8.

Assuming plane strain and effective material properties, a unit load is applied to the top of the free portion of the laminate. The displacement of the free portion, d_1, is then recorded. The displacement of the encased portion, d_2, is also recorded. The ratio of d_2 to d_1, η, given by

$$\eta = \frac{d_2 - d_1}{d_2}, \tag{10}$$

is used to calculate an effective stiffening value. The multiplier of encased material properties, η, is used to modify the the encased (potted) section of the laminate in the analyses of Section III.C.2. The material properties shown in Table 2 are used for the epoxy and aluminum. The effective properties of the laminate are calculated from the effective membrane properties as calculated by Classical Laminate Theory [27]. The η values calculated from the planar model for the QI and CTS cylinders are 1.53 and 1.55, respectively. All FE models discussed henceforth include the effects of end-potting.

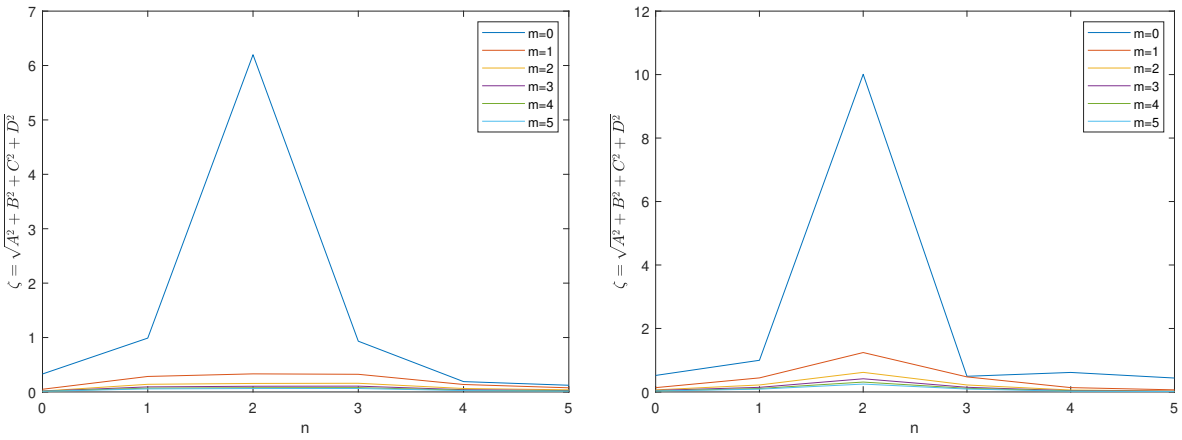

(a) **(b)**

Fig. 7 QI (a) and RTS (b) Fourier mode magnitudes.

Table 3 Pre-test predictions for linear and nonlinear buckling load, and axial stiffness for QI and RTS cylinders. Nonlinear buckling load is the value at which buckling occurs in the nonlinear FE model. Axial stiffness is calculated as the average gradient between 20 kN and buckling in the FE force-displacement graph.

Value	Unit	QI	RTS
Linear buckling load	kN	196.9	218.0
Nonlinear buckling load	kN	164.5	187.0
Axial stiffness	kN/mm	97.7	106.4

2. Pre-test prediction

The results of the end-potted analyses are shown in Table 3. The linear buckling load is calculated through a linear eigenvalue analysis within ABAQUS/CAE and uses a 'perfect' geometry cylinder (no imperfections). The 'perfect' geometry cylinder is the cylindrical best-fit as calculated from the CMM (see Fig. 4). The nonlinear buckling load is computed in ABAQUS/CAE through geometrically nonlinear static analyses with numerical stabilization.

IV. Axial Compression Test

In this section, the experimental setup and results are discussed. The test machine, pre-test procedure and results of both the QI and RTS cylinders are reported including data from the test machine, LVDTs, strain gauges and DIC. Both cylinders are tested twice beyond global buckling to investigate any hysteresis in the structural response.

A. Experimental Setup

A hydraulically operated, 500 kN four-pillar Dartec test machine was used to load the cylinders in axial compression with clamped boundary conditions enforced at either end through the application of the aforementioned end-potting. The load was applied through a top-down single pillar vertical displacement head. A custom loading plate was designed and manufactured to fit onto the testing machine as the standard loading head was too small for the ≈ 650 mm diameter epoxy/aluminum end-potting ring. After placing the cylinder in the test machine, the load head was brought down onto the cylinder until a nominal load was measured (i.e. the surfaces are touching). A feeler gauge was used between the cylinder end-potting and the loading plate to determine any out-of-parallelism. For both the QI and RTS cylinder, the feeler gauge indicated that the out-of-parallelism is between 0.05 mm and 0.1 mm, within the tolerances specified to the machine shop.

The test procedure included an initial loading of up to 20% of the predicted buckling displacement. Due to flatness and perpendicularity tolerances, both cylinders had a small settling region where one side of the cylinder was loaded before the rest of the cylinder. The prebuckling stiffness calculated in the initial loading cycle showed that both cylinders

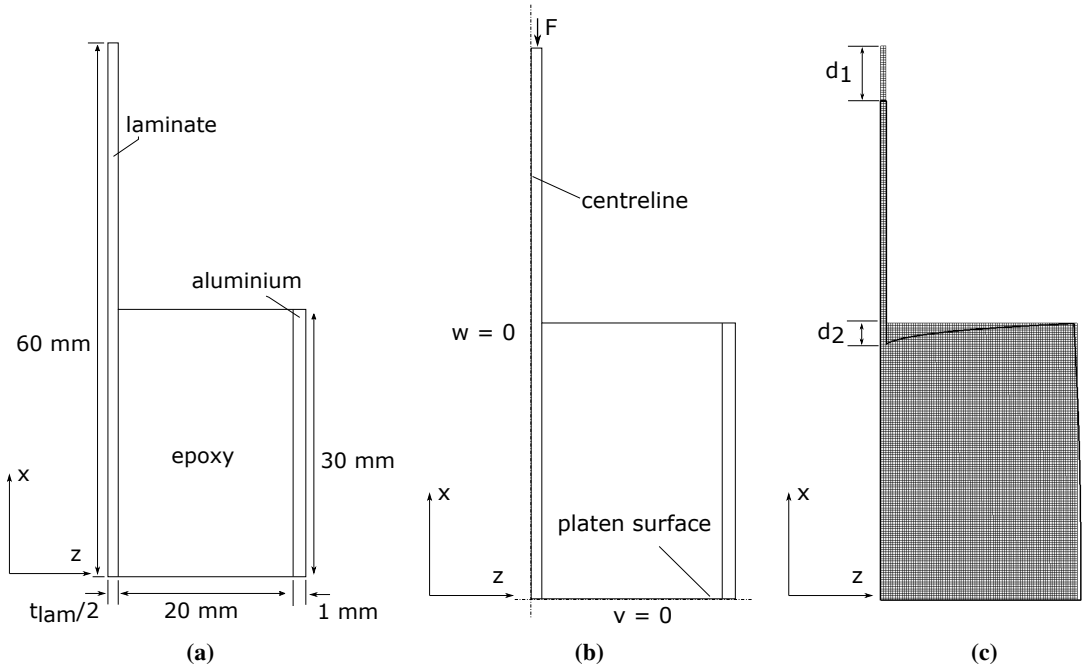

Fig. 8 Planar model of potting cross-section, with (a) geometry of planar model, (b) loading and boundary conditions of planar model and (c) deflection and displacements of planar model.

Table 4 Experimental results for both QI and RTS cylinders. Nonlinear buckling load is read from the Dartec test machine. Axial stiffness is calculated as the average gradient of the the four LVDTs for each cylinder between 20 kN and buckling. All values in the table are the average of the two tests.

Value	Unit	QI	RTS
Buckling load	kN	154.3	172.4
Axial stiffness	kN/mm	105.3	106.6

were close to model predictions, providing confidence in proceeding to the next stage of the test.

After the test loading, the first loading cycled commenced at a loading rate of 0.1 mm/min until global buckling. At the point of global buckling, the cylinder was carefully inspected for material failure (visible cracks or delaminations) and then unloaded and reloaded a second time to investigate any hysteresis in the structural response. In the reloading cycle the cylinder buckled globally again, was inspected, and any visible material failure noted. The cylinder was then taken to a deep post-buckled state until 2–3 mm of end-shortening was reached, at which point the cylinder was unloaded.

B. Experimental results

The experimental buckling loads and axial stiffnesses for both QI and RTS cylinder are collected in Table 4. As both cylinders are compression tested twice, the results presented and discussed refer to the first test cycle unless otherwise stated. For the QI cylinder, global buckling occurred at 154.3 kN, 94% of the predicted nonlinear buckling load. The experimental axial stiffness for the QI cylinder is within 8% of the predicted axial stiffness. The RTS cylinder buckled at 172.4 kN, 92% of the predicted nonlinear buckling load. The experimental axial stiffness for the RTS cylinder is within 0.2% of the predicted stiffness.

The force-displacement graphs of compression tests on the QI and RTS cylinder for test cycle 1 and 2 are shown in Figs. 9 and 10, respectively. Both graphs show the raw Dartec data for force and displacement measurements.

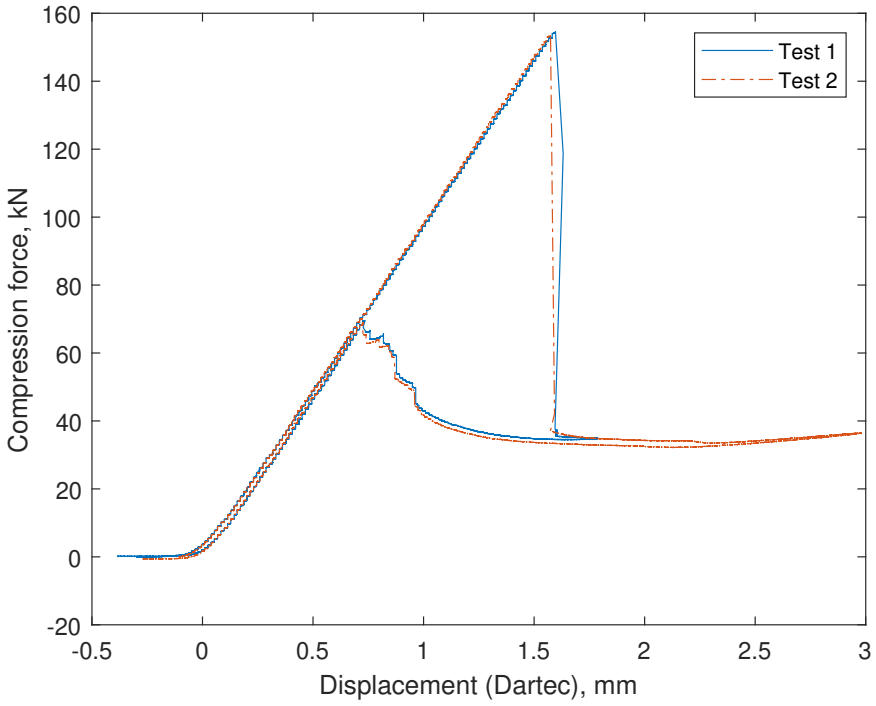

Fig. 9 Force-displacement graph of QI compression experiment for test cycle 1 and 2.

The experimental and predicted buckling modes are shown for both cylinders in Figs. 11 and 12, respectively. In the experiment, seven rows of two dimples were observed for both cylinders when global buckling occurred. These out-of-plane deformations were measured using the two-camera DIC system during the experiments. The white boxes in Figs. 11b and 12b represent the areas covered by the DIC camera system.

The experimental axial and hoop strain data for the QI cylinder for the first test cycle is compared against FE predictions in Figs. 17 and 18, respectively. Strain gauge G malfunctioned during the QI experiment and did not record data. Therefore, it is not plotted.

The LVDT data (four axial LVDTs) for both cylinders capture the loading eccentricity in the axial compression tests. The LVDT data for the first test cycle of QI and RTS cylinders are shown in Figs. 13 and 14, respectively. The offset between the four different curves in either plot indicate the presence of pre-bending in the test setup due to the residual non-flatness and non-perpendicularity of the loading surfaces with respect to the cylinder axis. As the tolerances achieved for the QI cylinder after machining were slightly better than the RTS cylinder, the level of pre-bending for QI cylinder is lower than for the RTS cylinder.

V. Interpretation and Correlation of Experimental Results

In this section, the experimental results are interpreted, correlated with finite element predictions, and discrepancies are then discussed. Rotations within the test setup are calculated and included into updated finite element predictions.

Both force-displacement graphs (Figs. 9 and 10) show a period of nonlinear settling at low levels of load and displacement. The nonlinear settling region occurs due to the unevenness of the loading surfaces. The LVDT data (Figs. 13 and 14) corroborate this interpretation as each LVDT shows different end-compression data, indicating that the compression was unevenly applied. This small eccentricity in loading is commonly observed in compression testing of cylinders [11]. Once quantified, the data can be post-processed further to better correlate FE predictions against experimental results by implementing the bending rotations into the FE model. The difference in displacements between opposing LVDT locations is used to calculate a rotation in this direction. The rotations are transposed to be in the global y- and z-directions, as defined by Fig. 6, and are applied to the model as a pre-loading step. The rotations in the y- and z-direction for test cycle 1 for the QI and RTS cylinder are shown in Figs. 15 and 16, respectively.

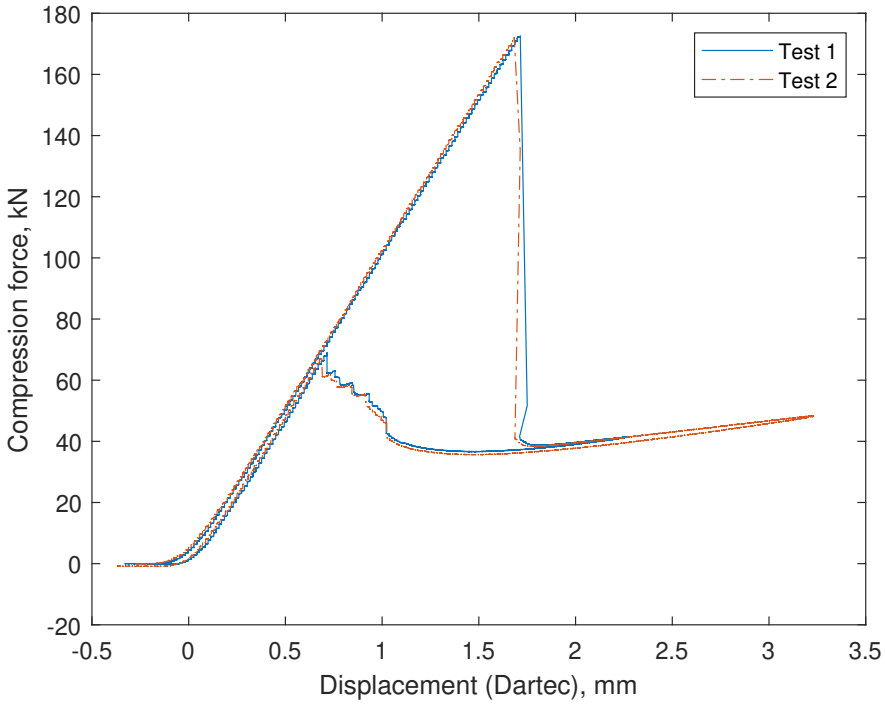

Fig. 10 Force-displacement graph of RTS compression experiment for test cycle 1 and 2.

Table 5 Average rotations caused by eccentric loading, rads

	QI	RTS
θ_y	9.73×10^{-5}	1.24×10^{-6}
θ_z	8.91×10^{-5}	-2.22×10^{-4}

The average rotations (shown in Table 5) across the linear pre-buckling region of loading are implemented into the FE model and used to update the nonlinear FE prediction of buckling load. The loading in the RTS cylinder is more eccentric than the QI cylinder due to the slightly inferior surface finish on the end-potting. When rotations are included in the FE model, the predicted buckling loads for both cylinders are lower than without rotations. The new predicted buckling loads, with previous predictions and experimental results, are shown in Table 6.

The new FE model buckling loads for the QI and RTS cylinders are 96% and 97% of the experimental buckling load, respectively. The axial stiffness is unaffected by the introduction of rotations. The remaining 4% and 3% differences, respectively, can be accounted for by considering material variability and fiber angle misalignment in the manufactured cylinders. Between test cycle 1 and test cycle 2, both cylinders exhibited no discernible material damage. Visual inspection after test cycle 1 indicated no cracks had formed during the buckling event. The almost identical test results for test cycles 1 and 2 for both QI and RTS cylinders (Figs. 9 and 10, respectively) indicate the buckling event did not induce damage (no hysteresis between loading and unloading) and that the cylinders were manufactured to high quality.

The post-buckled shape of the QI cylinders shows good shape correlation with the FE prediction. The maximum dimple deflection observed in the experiment, 16.8 mm, is 20% larger than predicted by FE. FE predicted two rows of eight dimples for the QI cylinder, one more dimple than shown in the experiment. The post-buckled shape of the RTS cylinder also shows good shape correlation with FE prediction. The maximum dimple deflection in the experiment, 18.8 mm, is 30% larger than that predicted by FE. FE predicted two rows of seven dimples, exactly the pattern observed in the experiment. Numerical stabilization within the nonlinear quasi-static solver is a likely cause of the mode shape discrepancy observed for the QI cylinder (seven vs. eight buckles). The fewer circumferential buckles corresponds to lower energy states in the multi-stable equilibrium landscape [28]. Stabilization applied in the FE solver introduces

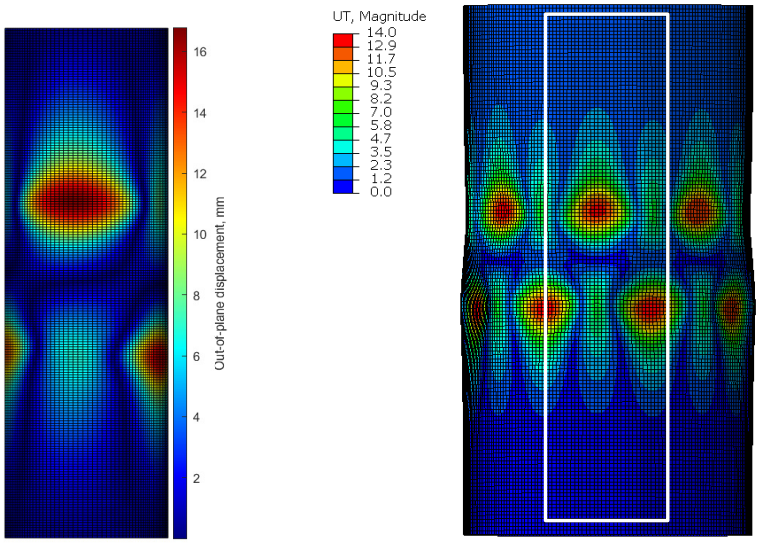

(a) **(b)**

Fig. 11 Experimental (a) and FE-predicted (b) post-buckled shapes and out-of-plane displacement magnitudes in mm for QI cylinder.

Table 6 Summary of buckling loads (perfect linear, perfect nonlinear, imperfect nonlinear, imperfect nonlinear with rotations, and experimental) for both QI and RTS cylinders. 'Perfect' and 'imperfect' refer to analyses that use the perfect, best-fit geometry of the shell or use the as-manufactured imperfections in the analysis, respectively.

	Value	Unit	QI	RTS
Predicted	Perfect linear buckling load	kN	196.9	218.0
	Perfect nonlinear buckling load	kN	192.9	210.0
	Imperfect nonlinear buckling load	kN	164.5	187.0
	Imperfect nonlinear buckling load with rotations	kN	160.7	177.5
Experiment	Buckling load	kN	154.3	172.4

artificial damping that can cause the solver to stabilize in a local energy minimum rather than transitioning all the way to the energy minimizer.

A simple metric to measure the imperfection sensitivity of the QI and RTS shells is to identify the linear KDF, the ratio of experimental buckling load to perfect linear buckling load. The linear KDFs are shown in Table 7. The RTS linear KDF is 0.792, 0.8% larger than the QI linear KDF of 0.786. Despite having an imperfection magnitude 8 times the average wall thickness and a greater loading imperfection, the RTS cylinder appears to be slightly more imperfection insensitive. However, the linear KDF uses the perfect linear buckling load which does not include the presence of a boundary layer, a feature that is known to reduce the load carrying ability of a cylinder [29] and be present in experiments. Therefore, to assess the imperfection sensitivity of the QI and RTS cylinder alone, the boundary layer must be included in both analyses. To consider this, a nonlinear KDF is calculated as the ratio between experimental buckling load and perfect nonlinear buckling load. The nonlinear KDFs are shown in Table 7. The RTS nonlinear KDF is 0.822, 2.5% higher than the QI nonlinear KDF 0.802. The comparison between nonlinear KDFs indicates that the RTS cylinder is more imperfection insensitive than the QI cylinder, despite having a larger geometric imperfection sensitivity magnitude and loading imperfection.

To further investigate the imperfection (in)sensitivity of the QI and RTS cylinders, the as-manufactured imperfections for both cylinders can be scaled and applied to the other design [30]. Currently, FE predictions cannot be directly compared as the scale and type of the imperfections measured for the QI and RTS cylinders are not the same (both cylinders had a general ovalization mode, but the ovalization was twice as large for the RTS cylinder). As the accuracy

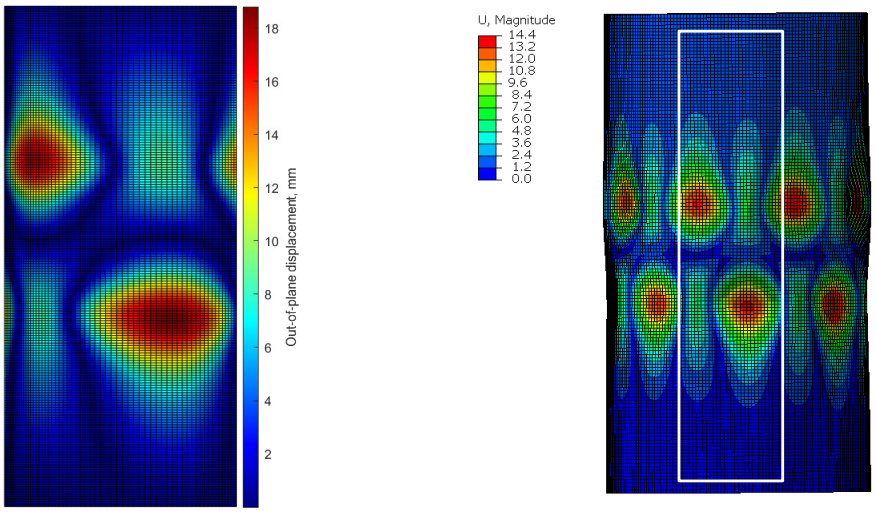

(a) **(b)**

Fig. 12 Experimental (a) and FE-predicted (b) post-buckled shapes and out-of-plane displacement magnitudes in mm for RTS cylinder.

Table 7 Linear and nonlinear KDF comparison.

KDF	QI	RTS
Linear KDF	0.786	0.792
Nonlinear KDF	0.802	0.822

of the FE models has been confirmed, we can impose the same imperfection for both cylinders and compare the results from the FE model. Therefore, the two factors that affect the buckling load of a cylinder with imperfections—the type of imperfection (combination of Fourier modes and end-rotation) and the scale of imperfection (maximum amplitude)—are modified by taking the QI measured imperfection and the RTS measured imperfection and applying them *vice versa* both in their original magnitude and by scaled magnitudes. As there are two types of imperfection (geometric and loading), the geometric imperfection is considered alone first, and then the loading imperfection is considered alongside the geometric imperfection. The combination of cylinder (QI or RTS) analyzed, the type of imperfection used (from QI or from RTS) and the scale of the imperfection applied (magnitude of the measured QI imperfection or magnitude of the measured RTS imperfection) is summarized in Table 8. The nonlinear FE KDF is the ratio between predicted nonlinear buckling load and perfect nonlinear buckling load.

Across all scenarios the actual RTS cylinder (combination 1) is less affected or even improved by changes in the imperfection shape or magnitude (combination 3 and 5) than the QI cylinder (combination 4 and 6), which is always

Table 8 Combination of cylinder design, imperfection type (ovalization) and scale of imperfection.

Combination	Cylinder	Ovalization	Scale	Nonlinear Buckling load, kN	Nonlinear FE KDF
1	RTS	RTS	RTS	187.0	0.890
2	QI	QI	QI	164.5	0.853
3	RTS	RTS	QI	204.1	0.972
4	QI	QI	RTS	141.5	0.734
5	RTS	QI	RTS	174.8	0.832
6	QI	RTS	QI	147.3	0.764

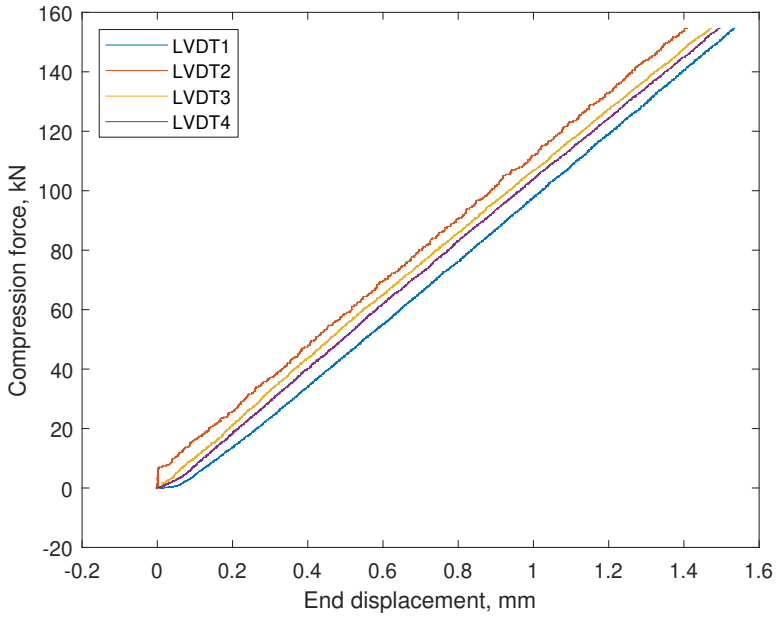

Fig. 13 LVDT data for the QI cylinder compression test cycle 1.

Table 9 Combination of cylinder design, imperfection type (ovalization and end rotation) and scale of imperfection.

Combination	Cylinder	Ovalization	End rotation	Scale	Nonlinear Buckling load, kN	Nonlinear FE KDF
7	RTS	RTS	RTS	RTS	177.5	0.845
8	QI	QI	QI	QI	160.7	0.833
9	RTS	RTS	RTS	QI	192.0	0.914
10	QI	QI	QI	RTS	140.1	0.726
11	RTS	QI	QI	RTS	173.4	0.826
12	QI	RTS	RTS	QI	143.9	0.746

lower than the actual tested cylinder (combination 2). On average, the nonlinear FE KDF for the RTS cylinder is 0.896, 13% higher than the average for the QI cylinder at 0.782. These preliminary results indicate that the RTS cylinder is more insensitive to geometric imperfections. When considering the loading imperfections (of the respective QI or RTS cylinder) with the geometric imperfections, all buckling loads are lower than without loading imperfections. The comparison between QI and RTS cylinders for various imperfections and scale are shown in Table 9.

Again, the RTS cylinder has a higher average nonlinear FE KDF (0.861) when compared to the average nonlinear FE KDF the QI cylinder (0.767). The results collated in Table 8 and 9 show that the RTS cylinder is more imperfection insensitive.

VI. Conclusion

Two large, high-quality composite cylinders were manufactured and tested in axial compression. The test results of a straight fiber (QI) cylinder and a tow-sheared (RTS) cylinder were compared and contrasted. The QI and RTS cylinder buckled within 3% and 4% of the predicted load (with manufacturing and loading imperfections), respectively. The experimental axial stiffnesses of the QI and RTS shell was within 8% and 0.2% of the predicted shell stiffnesses, respectively. Both cylinders show good correlation between the FE-predicted post-buckled shape and the experimental post-buckled shape. The RTS cylinder, despite having larger geometric imperfections and larger loading eccentricity, has a higher KDF and buckling load than the QI cylinder. In addition, when the smaller imperfection magnitude measured

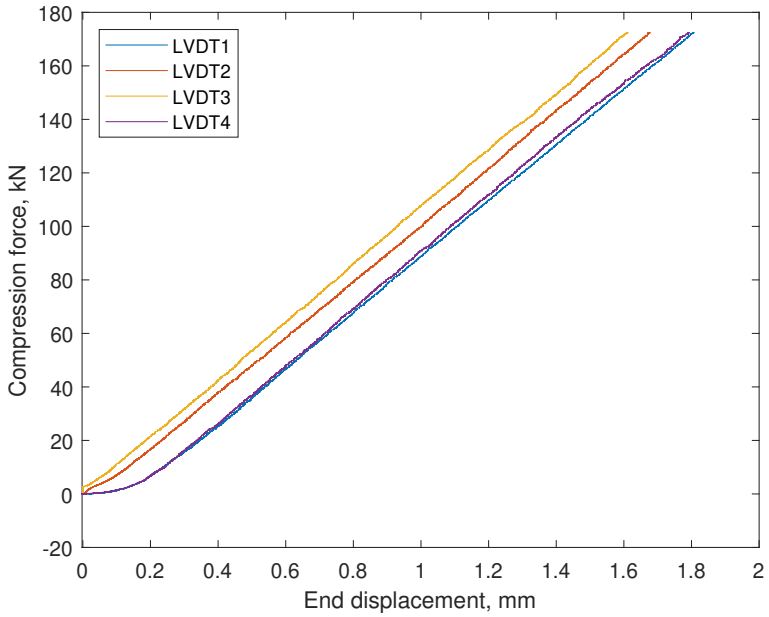

Fig. 14 LVDT data for the RTS cylinder compression test cycle 1.

for the QI cylinder is applied to imperfection signature measured for the RTS cylinder, the performance of the RTS cylinder is expected to improve by another 9%. Hence, if both cylinders had been manufactured with their respective imperfection signatures but identical imperfection magnitude (max out-of-plane deformation), then the RTS cylinder would have outperformed the QI cylinder even more. The lower sensitivity to changes in the imperfection mode in the FE analysis provides evidence that the RTS cylinder is less sensitive to typical geometric imperfections that occur during curing of composite cylinders than the baseline QI cylinder.

Appendix

The experimental axial and hoop strain data for the QI cylinder for the first test cycle is compared against FE predictions in Figs. 17 and 18, respectively. Strain gauge G malfunctioned during the QI experiment and did not record data. Therefore, only the FE prediction of strain gauge G is plotted. The experimental axial and hoop strain data for the RTS cylinder for the first test cycle is compared against FE predictions in Figs. 19 and 20, respectively.

Acknowledgments

We acknowledge the support and collaboration of iCOMAT Ltd., Bristol, UK in manufacturing the test specimens and the European Space Agency for funding this research. Special thanks go to Dr. K. Chauncey Wu at NASA Langley Research Center for his guidance in preparing and conducting manufacturing and experiments. R.L. Lincoln acknowledges the support of the EPSRC [Grant No. EP/L016028/1]. P.M. Weaver acknowledges the support of the Royal Society Wolfson Merit award and the Science Foundation Ireland for the award of a Research Professor grant [Varicomp: 15/RP/2773]. R.M.J. Groh acknowledges the support of the Royal Academy of Engineering under the Research Fellowship scheme [Grant No. RF/201718/17178]. The underlying data for this publication are available through the University of Bristol data repository.

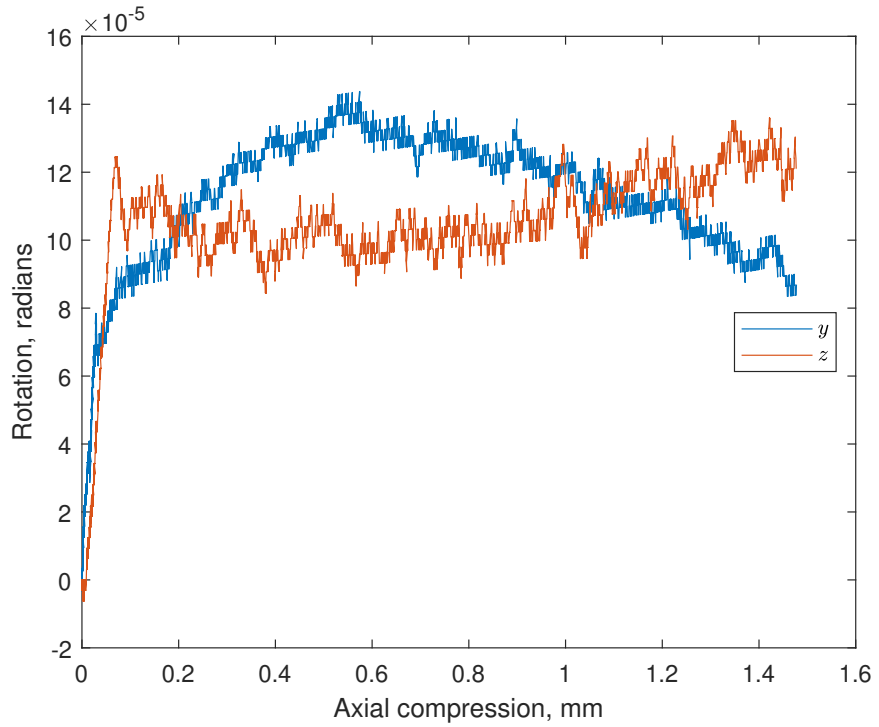

Fig. 15 Rotation in the *y*- and *z*-directions for the QI cylinder, test cycle 1.

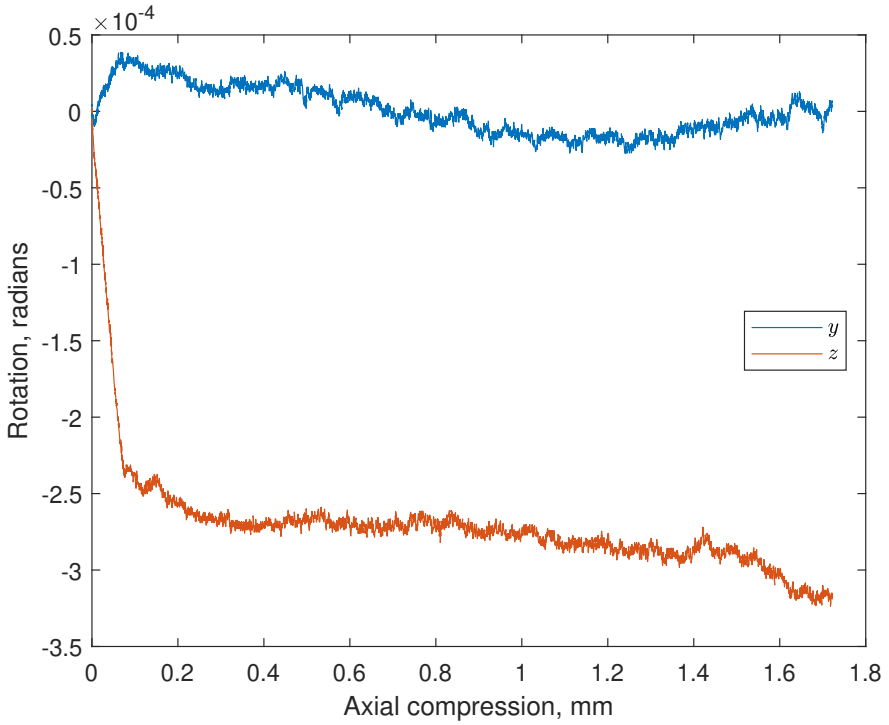

Fig. 16 Rotation in the *y*- and *z*-directions for the RTS cylinder, test cycle 1.

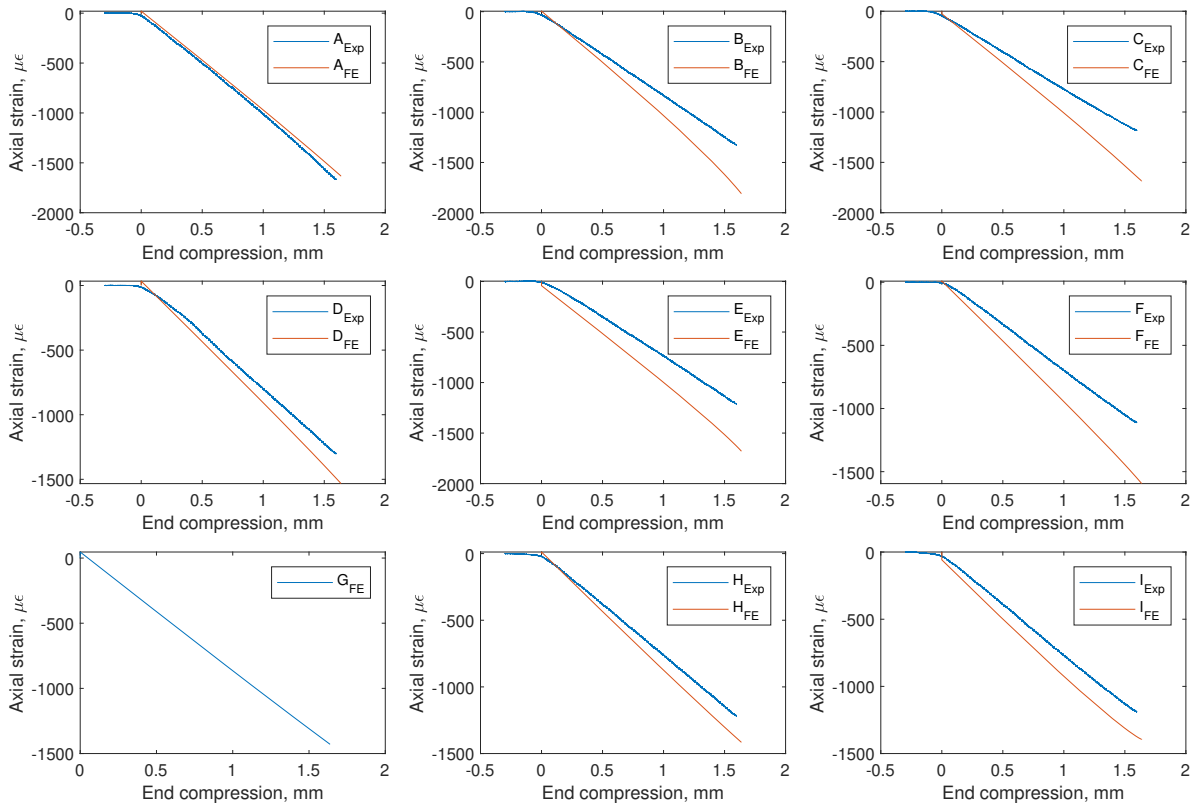

Fig. 17 Experimental (Exp) and FE-predicted (FE) axial strain data for each strain gauge of the QI cylinder.

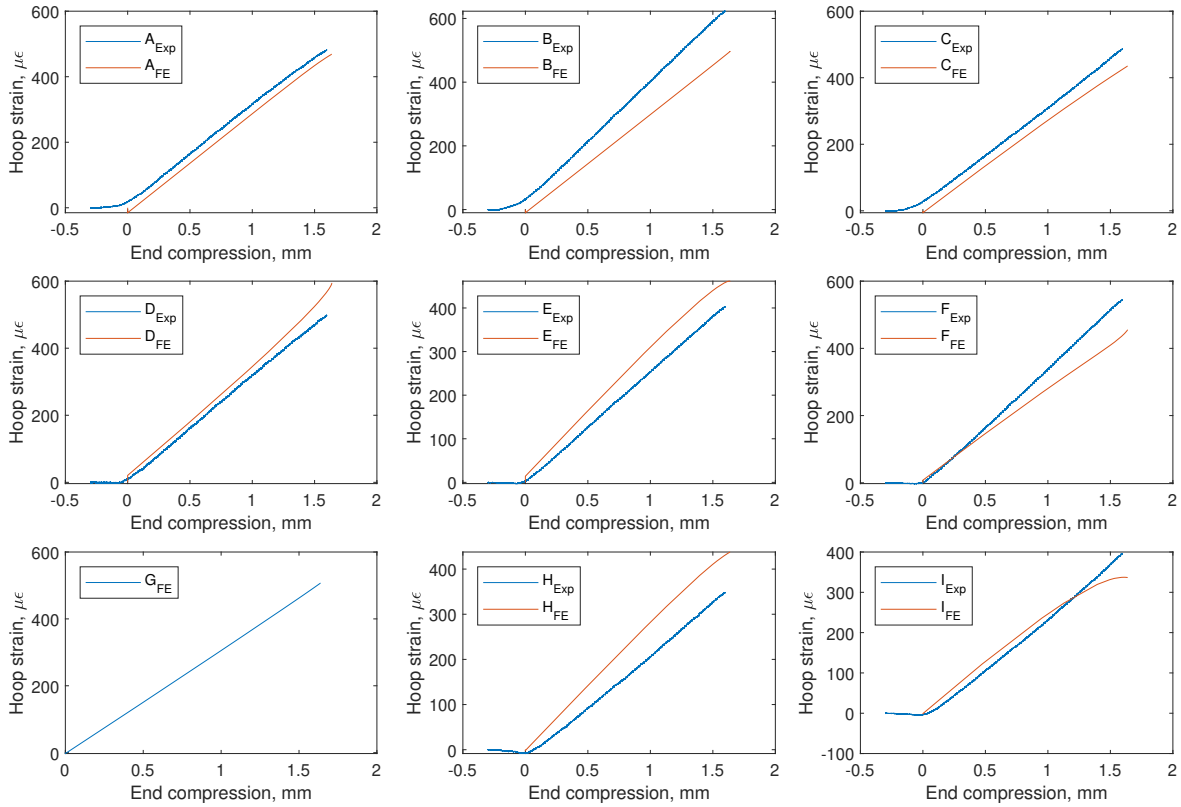

Fig. 18 Experimental (Exp) and FE-predicted (FE) hoop strain data for each strain gauge of the QI cylinder.

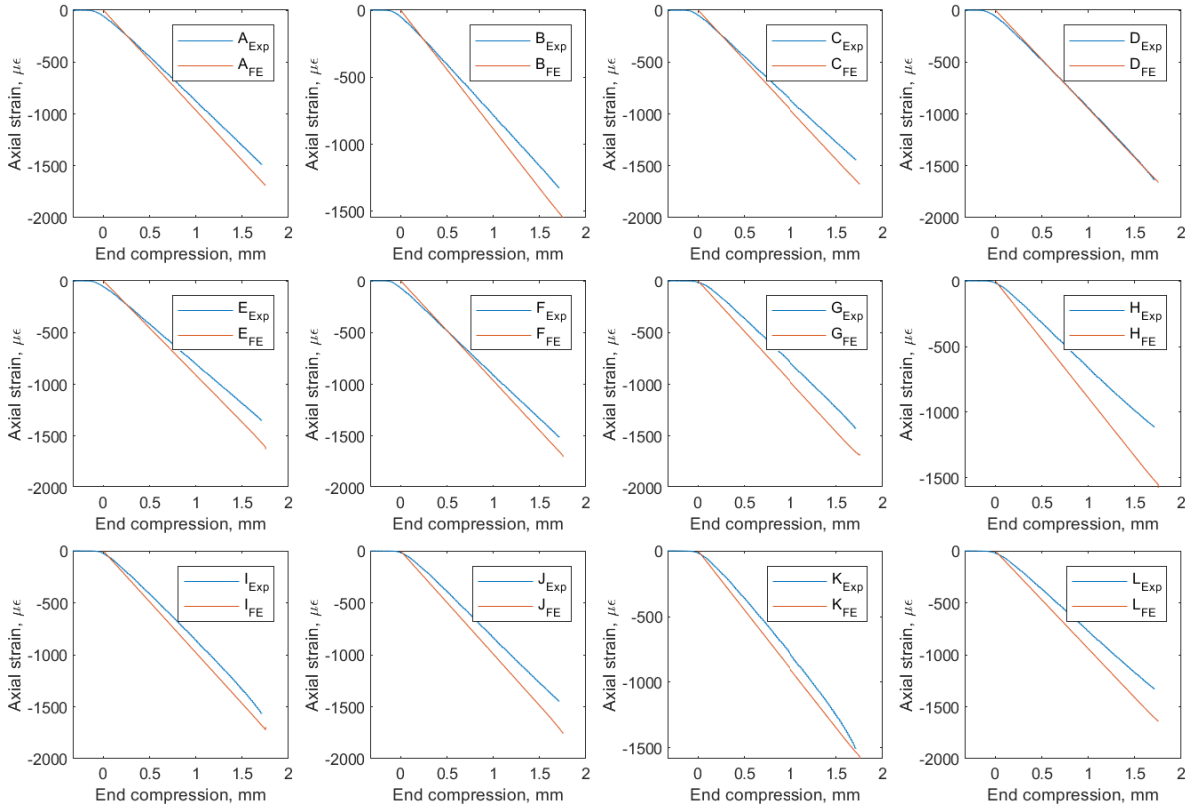

Fig. 19 Experimental (Exp) and FE-predicted (FE) axial strain data for each strain gauge of the RTS cylinder.

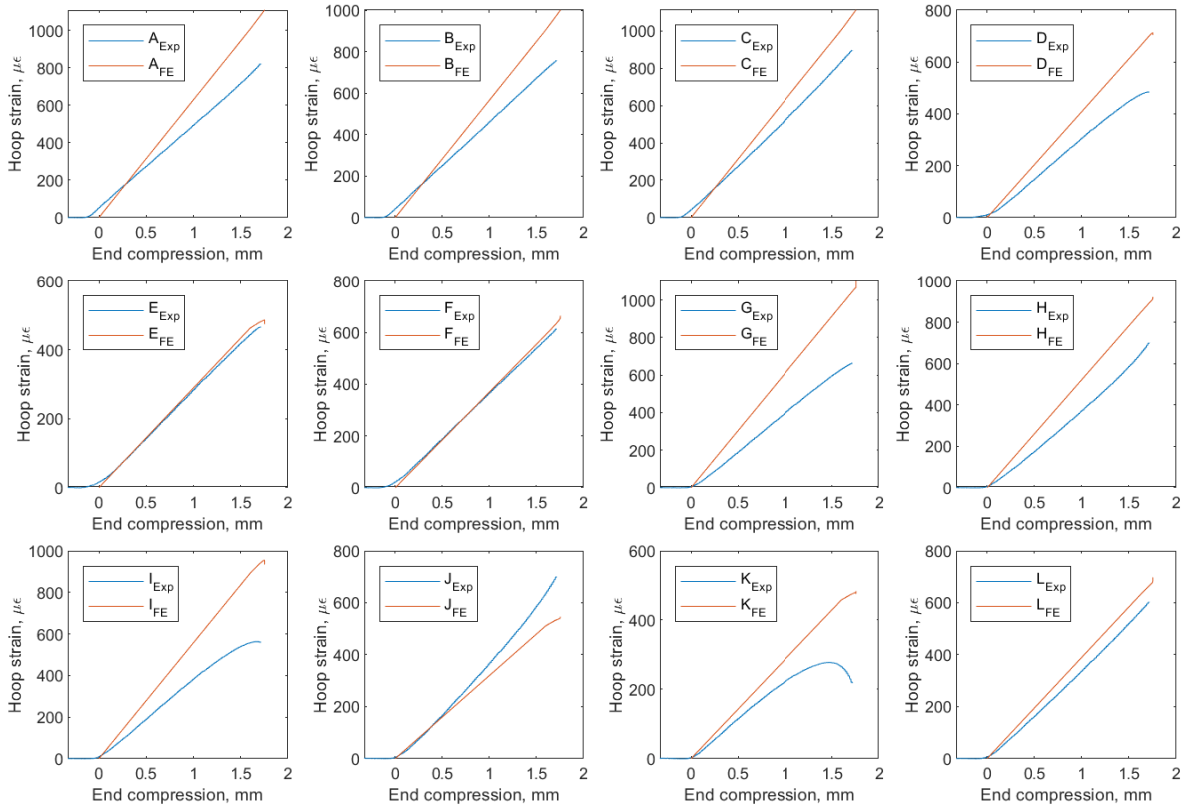

Fig. 20 Experimental (Exp) and FE-predicted (FE) hoop strain data for each strain gauge of the RTS cylinder.

References

[1] National Aeronautics and Space Administration, "Composite Cryotank Technologies and Demonstration," Tech. rep., NASA, 2013.

[2] McCarville, D. A., Guzman, J. C., Dillon, A. K., Jackson, J. R., and Birkland, J. O., "Design, manufacture and test of cryotank components," *Comprehensive Composite Materials II*, Vol. 3, 2018, pp. 153–179. https://doi.org/10.1016/B978-0-12-803581-8.09958-6.

[3] Kim, B. C., Hazra, K., Weaver, P., and Potter, K., "Limitations of fibre placement techniques for variable angle tow composites and their process-induced defects," *18th International Conferences on Composite Materials*, Jeju, Korea, 2011, pp. 1–6.

[4] Kim, B. C., Potter, K., and Weaver, P. M., "Continuous tow shearing for manufacturing variable angle tow composites," *Composites Part A: Applied Science and Manufacturing*, Vol. 43, No. 8, 2012, pp. 1347–1356. https://doi.org/10.1016/j.compositesa.2012.02.024.

[5] iCOMAT Ltd., "iCOMAT Ltd," , 2021. URL https://www.icomat.co.uk/.

[6] Kim, B. C., Weaver, P. M., and Potter, K., "Manufacturing characteristics of the continuous tow shearing method for manufacturing of variable angle tow composites," *Composites Part A: Applied Science and Manufacturing*, Vol. 61, 2014, pp. 141–151. https://doi.org/10.1016/j.compositesa.2014.02.019.

[7] Lincoln, R. L., Weaver, P. M., Pirrera, A., and Groh, R. M., "Optimization of imperfection-insensitive continuous tow sheared rocket launch structures," *AIAA Scitech 2021 Forum*, Vol. 1, No. January, 2021, pp. 1–19. https://doi.org/10.2514/6.2021-0202.

[8] Lincoln, R., Weaver, P., Pirrera, A., and Groh, R., "Imperfection-Insensitive Continuous Tow-Sheared Cylinders," *Composite Structures*, Vol. 260, No. March, 2021, p. 113445. URL http://hdl.handle.net/1983/192c7097-979b-4413-8daf-fd75b6815909.

[9] Hyer, M., and Charette, R., "Use of curvilinear fiber format in composite structure design," *AIAA Journal*, Vol. 29, No. 6, 1991, pp. 1011–1015.

[10] White, S. C., and Weaver, P. M., "Towards imperfection insensitive buckling response of shell structures-shells with plate-like post-buckled responses," *The Aeronautical Journal*, Vol. 120, No. 1224, 2016, pp. 233–253. https://doi.org/10.1017/aer.2015.14, URL https://www.cambridge.org/core/product/identifier/S0001924015000147/type/journal_article.

[11] Wu, K. C., Stanford, B. K., Hrinda, G. A., Wang, Z., Martin, R. A., and Kim, H. A., "Structural Assessment of Advanced Tow-Steered Shells," *54th AIAA/ASME/ASCE/AHS/ASC Structures, Structural Dynamics, and Materials Conference*, Boston, Massachusetts, 2013, pp. 1–20. https://doi.org/10.2514/6.2013-1769.

[12] White, S. C., Weaver, P. M., and Wu, K. C., "Post-buckling analyses of variable-stiffness composite cylinders in axial compression," *Composite Structures*, Vol. 123, 2015, pp. 190–203. https://doi.org/10.1016/j.compstruct.2014.12.013, URL http://dx.doi.org/10.1016/j.compstruct.2014.12.013.

[13] Wu, K. C., Turpin, J. D., Stanford, B. K., and Martin, R. A., "Structural performance of advanced composite tow-steered shells with cutouts," *55th AIAA/ASMe/ASCE/AHS/SC Structures, Structural Dynamics, and Materials Conference*, 2014, pp. 1–20. https://doi.org/10.2514/6.2014-1056.

[14] Wu, K. C., Turpin, J. D., Gardner, N. W., Stanford, B., and Martin, R. A., "Structural Characterization of Advanced Composite Tow-Steered Shells with Large Cutouts," *55th AIAA/ASME/ASCE/AHS/SC Structures, Structural Dynamics, and Materials Conference*, 2014, pp. 1–20. https://doi.org/10.2514/6.2015-0966.

[15] Blom, A. W., Rassaian, M., Stickler, P. B., and Gürdal, Z., "Bending test of a variable-stiffness fiber-reinforced composite cylinder," *Collection of Technical Papers - AIAA/ASME/ASCE/AHS/ASC Structures, Structural Dynamics and Materials Conference*, 2010, pp. 1–21. https://doi.org/10.2514/6.2010-2600, URL http://arc.aiaa.org.

[16] Gurdal, Z., and Olmedo, R., "In-plane response of laminates with spatially varying fiber orientations - Variable stiffness concept," *AIAA Journal*, Vol. 31, No. 4, 1993, pp. 751–758. https://doi.org/10.2514/3.11613.

[17] Marlett, K., Ng, Y., and Tomblin, J., "Hexcel 8552 IM7 Unidirectional Prepreg Qualification Material Property Data Report," Tech. rep., National Institute for Aviation Research, Wichita, Kansas, 2011.

[18] Elishakoff, I., Van Manent, S., Vermeulen, P. G., and Arbocz, J., "First-order second-moment analysis of the buckling of shells with random imperfections," *AIAA Journal*, Vol. 25, No. 8, 1987, pp. 1113–1117. https://doi.org/10.2514/3.9751.

[19] Kriegesmann, B., "Probabilistic design of thin-walled fiber composite structures," Ph.D. thesis, Gottfried Wilhelm Leibniz University Hannover, 2012.

[20] Wagner, R., "Robust design of buckling critical thin-walled shell structures," *DLR Deutsches Zentrum fur Luft- und Raumfahrt e.V. - Forschungsberichte*, Vol. 2019-Janua, No. 14, 2019, pp. 1–127. https://doi.org/10.13140/RG.2.2.15095.16801.

[21] Wagner, H. N., Hühne, C., and Janssen, M., "Buckling of cylindrical shells under axial compression with loading imperfections: An experimental and numerical campaign on low knockdown factors," *Thin-Walled Structures*, Vol. 151, 2020. https://doi.org/10.1016/j.tws.2020.106764.

[22] Kriegesmann, B., Rolfes, R., Hühne, C., Teßmer, J., and Arbocz, J., "Probabilistic design of axially compressed composite cylinders with geometric and loading imperfections," *International Journal of Structural Stability and Dynamics*, Vol. 10, No. 4, 2010, pp. 623–644. https://doi.org/10.1142/S0219455410003658.

[23] Vries, J. D., "The Imperfection Data Bank and its Applications," Ph.D. thesis, Delft University, 2009.

[24] Wu, K. C., Tatting, B. F., Smith, B. H., Stevens, R. S., Occhipinti, G. P., Swift, J. B., Achary, D. C., and Thornburgh, R. P., "Design and manufacturing of tow-steered composite shells using fiber placement," *AIAA/ASME/ASCE/AHS/ASC Structures, Structural Dynamics and Materials Conference*, 2009, pp. 1–18. https://doi.org/10.2514/6.2009-2700.

[25] Arbocz, J., and Abramovich, H., "The initial imperfection data bank at the Delft University of Technology: Part I," , 1979. URL http://www.narcis.nl/publication/RecordID/oai:tudelft.nl:uuid:89f6a74c-32c2-4605-88d5-2a70692b5857.

[26] Hilburger, M. W., and Starnes, J. H., "Effects of imperfections of the buckling response of composite shells," *Thin-Walled Structures*, Vol. 42, No. 3, 2004, pp. 369–397. https://doi.org/10.1016/j.tws.2003.09.001.

[27] Jones, R. M., *Mechanics of Composite Materials*, 2nd ed., Taylor & Francis Ltd., 1999.

[28] Groh, R. M., Hunt, G. W., and Pirrera, A., "Snaking and laddering in axially compressed cylinders," *International Journal of Mechanical Sciences*, Vol. 196, No. December 2020, 2021. https://doi.org/10.1016/j.ijmecsci.2021.106297.

[29] Arbocz, J., and Babcock, C., "Effect of General Imperfections on the Buckling of Cylindrical Shell," *ASME-Paper 69-APM-6*, 1969.

[30] Wu, K. C., Farrokh, B., Stanford, B., and Weaver, P., "Imperfection Insensitivity Analyses of Advanced Composite Tow-Steered Shells," *57th AIAA/ASCE/AHS/ASC Structures, Structural Dynamics, and Materials Conference*, 2016, pp. 1–16. https://doi.org/10.2514/6.2016-1498.